Title

Experimental depth dose curves of a 67.5 MeV proton beam for benchmarking and validation of Monte Carlo simulation

Journal

Medical Physics, 42(7)

ISSN

0094-2405

Authors

Faddegon, Bruce A
Shin, Jungwook
Castenada, Carlos M
et al.

Publication Date

2015-06-17

DOI

10.1118/1.4922501

Peer reviewed

Experimental depth dose curves of a 67.5 MeV proton beam for benchmarking and validation of Monte Carlo simulation

Bruce A. Faddegon[a)]
Department of Radiation Oncology, University of California San Francisco, 1600 Divisadero Street, Suite H1031, San Francisco, California 94143

Jungwook Shin
St. Jude Children's Research Hospital, 252 Danny Thomas Place, Memphis, Tennessee 38105

Carlos M. Castenada
Crocker Nuclear Laboratory, University of California Davis, 1 Shields Avenue, Davis, California 95616

José Ramos-Méndez and Inder K. Daftari
Department of Radiation Oncology, University of California San Francisco, 1600 Divisadero Street, Suite H1031, San Francisco, California 94143

(Received 4 June 2014; revised 6 May 2015; accepted for publication 25 May 2015; published 17 June 2015)

Purpose: To measure depth dose curves for a 67.5 ± 0.1 MeV proton beam for benchmarking and validation of Monte Carlo simulation.
Methods: Depth dose curves were measured in 2 beam lines. Protons in the raw beam line traversed a Ta scattering foil, 0.1016 or 0.381 mm thick, a secondary emission monitor comprised of thin Al foils, and a thin Kapton exit window. The beam energy and peak width and the composition and density of material traversed by the beam were known with sufficient accuracy to permit benchmark quality measurements. Diodes for charged particle dosimetry from two different manufacturers were used to scan the depth dose curves with 0.003 mm depth reproducibility in a water tank placed 300 mm from the exit window. Depth in water was determined with an uncertainty of 0.15 mm, including the uncertainty in the water equivalent depth of the sensitive volume of the detector. Parallel-plate chambers were used to verify the accuracy of the shape of the Bragg peak and the peak-to-plateau ratio measured with the diodes. The uncertainty in the measured peak-to-plateau ratio was 4%. Depth dose curves were also measured with a diode for a Bragg curve and treatment beam spread out Bragg peak (SOBP) on the beam line used for eye treatment. The measurements were compared to Monte Carlo simulation done with GEANT4 using TOPAS.
Results: The 80% dose at the distal side of the Bragg peak for the thinner foil was at 37.47 ± 0.11 mm (average of measurement with diodes from two different manufacturers), compared to the simulated value of 37.20 mm. The 80% dose for the thicker foil was at 35.08 ± 0.15 mm, compared to the simulated value of 34.90 mm. The measured peak-to-plateau ratio was within one standard deviation experimental uncertainty of the simulated result for the thinnest foil and two standard deviations for the thickest foil. It was necessary to include the collimation in the simulation, which had a more pronounced effect on the peak-to-plateau ratio for the thicker foil. The treatment beam, being unfocussed, had a broader Bragg peak than the raw beam. A 1.3 ± 0.1 MeV FWHM peak width in the energy distribution was used in the simulation to match the Bragg peak width. An additional 1.3–2.24 mm of water in the water column was required over the nominal values to match the measured depth penetration.
Conclusions: The proton Bragg curve measured for the 0.1016 mm thick Ta foil provided the most accurate benchmark, having a low contribution of proton scatter from upstream of the water tank. The accuracy was 0.15% in measured beam energy and 0.3% in measured depth penetration at the Bragg peak. The depth of the distal edge of the Bragg peak in the simulation fell short of measurement, suggesting that the mean ionization potential of water is 2–5 eV higher than the 78 eV used in the stopping power calculation for the simulation. The eye treatment beam line depth dose curves provide validation of Monte Carlo simulation of a Bragg curve and SOBP with 4%/2 mm accuracy.
 [http://dx.doi.org/10.1118/1.4922501]

Key words: proton, benchmark, Bragg peak, SOBP, Monte Carlo

1. INTRODUCTION

Proton radiotherapy is an established medical procedure for treating a wide range of cancers. The continued installation of proton treatment facilities[1,2] is a strong motivation to establish as accurate a treatment as can be reasonably achieved. This requires accurate dose calculation in treatment planning. The Monte Carlo method is increasingly used in x-ray and

electron radiotherapy.[3] Research systems provide a clinically advantageous improvement in the accuracy of dose calculation for proton therapy.[4] Such systems are able to simulate the measured dose distributions, given accurate knowledge of the material comprising the phantom or patient, with an accuracy of 1–2 mm in the position of the distal edge of the dose distribution.[5] Monte Carlo simulation is coming into use for dose calculation in treatment planning, as practical limitations such as calculation time [a day or two to simulate a clinical proton treatment with TOPAS (Ref. 6) on a single standard PC (Ref. 7)] may no longer be an obstacle in planning proton treatments, with the advent of Monte Carlo simulation using cloud computing[8,9] and/or GPU technology.[7,10] Dose delivery with 1–2 mm accuracy is both clinically advantageous and conceivably achievable with imaging techniques used to verify the accuracy of the position of the patient and internal organs and structures at the time of treatment.[11] In order to achieve such accuracy in proton range calculation, the mean ionization potential (I-value) of water and human tissues, as well as of the composition of organs and tissue, must be determined with sufficient accuracy.[12]

Published Monte Carlo simulations of proton depth dose curves generally have used energy tuning to match depth penetration. The simulated depth dose curves generally agree with measurements within 1–2 mm, including beams with different ranges and spread out Bragg peak (SOBP) widths.[13,14] Submillimeter agreement, with energy tuning, has been achieved for short range protons used in eye therapy.[15–18]

The main purpose of this study is to measure the Bragg curve of a proton beam with submillimeter accuracy in depth penetration, with minimal material in the beam line, and with energy known to the same or higher accuracy than the depth. The measurement is intended for researchers and clinical practitioners to benchmark the Monte Carlo tool they use in proton therapy dose calculation. The benchmark provides a measure of the I-value for water required to obtain a submillimeter match of the depth penetration in the Monte Carlo simulation. The result additionally serves to help determine the accuracy of the energy derived from the common practice of matching the range in the simulation to the measured range for the clinical proton beam. The secondary purpose of this study is to provide experimental validation of Monte Carlo systems with a Bragg curve and SOBP measured in a clinical beam line.

The raw beam benchmarks reported in this paper are 67.5 ± 0.1 MeV Bragg curves measured with an uncertainty of 0.15 mm in depth on a beam line with two different Ta scattering foils and minimal material in the beam path. The thickness, density, and composition of this material were known sufficiently to make a negligible contribution to the uncertainty in the simulated position of the Bragg peak (Fig. 1). Depth dose curves measured on the treatment beam used for eye proton therapy, in operation since 1996 (Fig. 2), are also reported for both the Bragg peak and a nominal 20 mm SOBP. Monte Carlo simulations are used in this study to calculate the silicon-to-air stopping power ratio for the clinical beam, to provide uncertainty estimates for assumptions including radial symmetry, and to show the agreement achieved between measurement and simulation for the Bragg curve benchmarks and clinical beam validation results.

2. MATERIALS AND METHOD

2.A. Proton beam and beam lines

Measurements were performed with the 67.5 MeV proton beam accelerated by the Crocker Lab cyclotron installed at the University of California Davis. Beam energy may be calibrated using range-energy tables.[19] However, an independent determination of the beam energy is preferred for the experimental benchmark. The beam energy had been previously measured on the raw beam line using a time of flight (TOF) system.[20] Briefly, the system consisted of a plastic scintillator to detect the gamma rays produced in two beam stops that intercepted the beam. The signals from the scintillators were used to measure the time a proton travels between the two stops. With this method, the energy of the beam exiting the cyclotron (prior to traversing the scattering foil) was determined to be 67.5 ± 0.1 MeV. The TOF system is used routinely to verify the beam energy.

The beam was either directed into the raw beam line (Fig. 1) or the eye treatment beam line (Fig. 2). Detailed geometry information for both beam lines is given in the Appendix. The eye treatment beam line is as described previously.[21,22] The spot observed on radiochromic film (Gafchromic EBT3) placed 47.5 cm downstream of the foil position (TA in Fig. 1), with no foil in the beam, was a 5 × 10 mm oval. The proton energy distribution at the exit window of the raw beam line was previously measured with a CsI detector. The beam energy from the CsI measurement was not used, as it was not as accurate as the energy from the TOF system. The width of the peak in the CsI pulse height distribution included intrinsic peak broadening. Thus, the width of the peak of 0.4 MeV (0.6%) is an upper limit on the FWHM of the peak in the

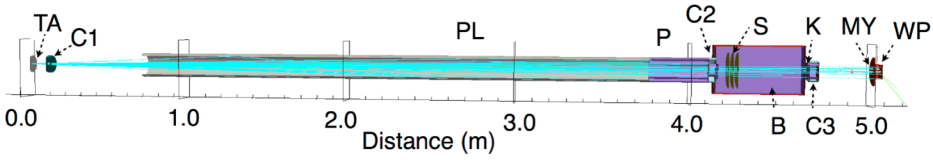

FIG. 1. Raw beam line used for benchmark measurements showing the Ta scattering foil (TA), the four sequentially placed collimating elements of the carbon collimator (C1), beam plug (PL), beam pipe (P), and second collimator (C2), the secondary emission monitor (S) enclosed in an evacuated box (B), the exit window (K) with the third collimator (C3), where the beam passes out of vacuum into air, and the Mylar window (MY) with water phantom (WP). See Table I in the Appendix for detailed geometry. A few simulated proton tracks are shown.

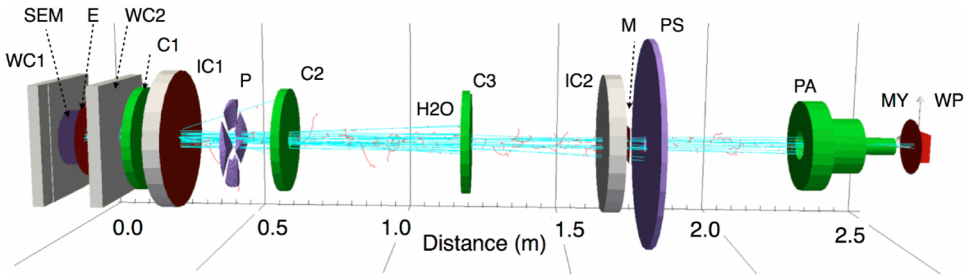

FIG. 2. Crocker Lab beam line used for eye treatment, showing the wire chambers (WC1 and WC2), secondary emission monitor (SEM), exit window (E), collimators (C1, C2, and C3), ion chambers (IC1 and IC2), range modulator wheel (P), water column (H2O), mirror (M), patient shield (PS), patient assembly (PA), Mylar window (MY), and water phantom (WP). See Table III in the Appendix for detailed geometry.

proton energy distribution for the raw beam line with no Ta foil. A pair of quadrupole magnets was used to focus the beam in the raw beam line. The magnets were turned off for the eye treatment beam line. This resulted in a considerably broader Bragg peak, due to the broader peak in the energy distribution of the beam from the cyclotron. Thus, the upper limit in peak FWHM does not apply to the eye treatment beam line.

Depth dose curves were measured in a water tank, a 360 mm wide cube with a 0.25 mm thick Mylar wall on the upstream side and 10 mm thick acrylic walls on the other sides. Lasers were used to center the detector on the beam axis, with the Mylar wall set perpendicular to the beam axis. The water tank was positioned 300 mm from the exit window in the raw beam line and 50 mm from the downstream end of the patient assembly in the eye treatment beam line.

2.B. Measurements

Diode detectors and parallel-plate ion chambers were used to measure the depth ionization curves.[23] The dose to a Bragg–Gray cavity of water embedded in a detector is the product of the dose to the material that comprises the detector sensitive volume with the material-to-water stopping power ratio (SPR) (see, for example, the theory presented in the AAPM TG-21 protocol for dose calibration,[24] which forms the basis for the current AAPM dose calibration protocol[25]). The depth ionization curves measured in both beam lines were converted to depth dose curves using published 70 MeV proton water-to-air and water-to-silicon SPRs calculated with the Monte Carlo method using the GEANT4-based code GAMOS.[26] The SPRs are published for discrete energies (depth penetration) and need to be adjusted to match the energy (range) of the particular beam before being applied. The published SPRs were shifted to match the measured depth of 80% dose on the distal side of the Bragg peak. The published SPRs calculated with GAMOS are for monoenergetic beams. This proved to be sufficient for the Bragg curves, but not the broad energy distribution used to generate a SOBP. Thus, the depth ionization curve measured for the SOBP in the eye treatment beam line with a diode was converted using SPRs calculated with a full simulation of the beam line using TOPAS.[6] A correction for the water-to-silicon SPR is needed for the SOBP since it varies by 11% from the surface to the depth of 80% dose on the distal side of the Bragg peak as calculated with TOPAS.

The benchmark Bragg curves, the eye treatment beam line Bragg curve, and SOBP depth dose curve reported were measured with diodes. The diodes were from two different manufacturers, a PTW diode (PTW Dosimetry Diode E Type 60012) and an EFD diode (IBA Dosimetry AB EFD-3G). The diode was positioned with the diode surface, coincident with the surface of the Mylar wall as follows. The detector was firmly held in place in the water tank, connected rigidly to a motorized stage (Newport ILS100cc translation stage 100 mm) and bolted to the top of one of the water tank walls. The stage moved in 3 μm steps with a reproducibility of 3 μm according to manufacturer specification. The diode was positioned in the water tank on the beam axis with lasers and within a few millimeters of the Mylar wall (Fig. 3). A distance gauge with a scale of 0.0254 mm per scale division was gently pressed against the Mylar window and held firmly in place on a retort stand, with the gauge reading not more than 0.1 mm to avoid deforming the Mylar wall, which covered the entire side of the water tank. The detector was moved in small increments and reduced to 0.05 mm steps when the detector was very close to the wall, until the scale on the gauge moved, indicating the detector was touching the wall. The detector was then moved back half of the final increment and this was the zero position. This approach accounts for the slight bending of the Mylar wall outward when the water was added. The accuracy of the

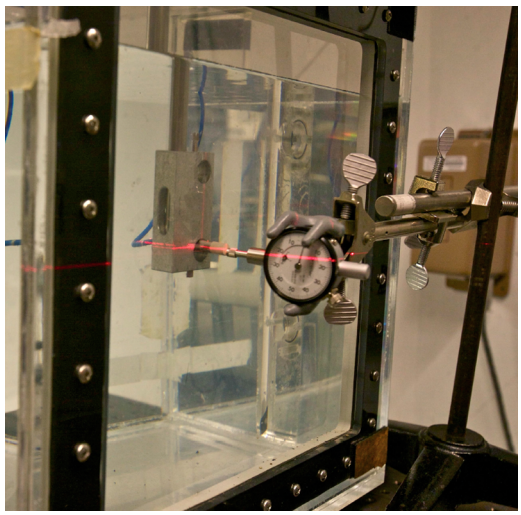

FIG. 3. Setup for positioning diode at the surface of the Mylar wall.

depth of the surface of the detector was 0.1 mm or better. The depth of the measurement point was calculated as a sum of 3 thicknesses: the thickness of the Mylar wall in mass per unit area, added to the depth of the surface of the detector (as read from the motor controller), and added to the depth of the sensitive (or active) volume of the detector in mass per unit area (that is, corrected for mass density). The accuracy of this positioning method, including the correction for the point of measurement, was validated by comparing the position of the distal edge of the Bragg peak measured with the two different diodes.

The depth of the surface of the silicon sensitive volume was measured on microCT scans taken from the diodes at UCSF. The measured depth from the image was 0.58 ± 0.08 mm for the PTW diode, in agreement with the manufacturer specification of 0.60 ± 0.20 mm. The measured depth was 0.56 ± 0.08 mm for the EFD diode, compared to the manufacturer specification of 0.58 mm (uncertainty not specified by manufacturer). The material is a combination of plastic of 1.045 g/cm^3 and epoxy according to manufacturer specification for the PTW diode. Epoxy has a density in the range of 1.1–1.4 g/cm^3. The average density of the material above the silicon in both diodes was estimated to be 1.2 ± 0.1 g/cm^3. This gives a water equivalent depth (from the diode surface to the surface of the sensitive volume) of 0.71 ± 0.15 mm for the PTW diode and 0.68 ± 0.15 mm for the EFD diode, where the uncertainty estimates includes the 0.1 mm uncertainty in the position of the surface of the diode relative to the Mylar window, uncertainties added in quadrature. The thickness of the sensitive volume (0.0025 mm PTW, 0.06 mm EFD, both manufacturer specifications) was not taken into account.

Measurements commenced with the diode surface abutting the Mylar window (with minimal distortion of the window), then proceeded with the diode being moved deeper into the water. The Bragg peak was found with a course step size then scanned with finer steps. For the single case of the PTW diode when the thinner foil was in the beam, the measurement at a point near the surface was repeated to evaluate a possible reduction in diode sensitivity with dose.[27,28]

A separate set of measurements was done in the raw beam with parallel-plate chambers. Potentially significant uncertainties when using diodes include the uncertainty in the mean restricted water-to-silicon mass SPR at the Bragg peak relative to that at the plateau.[29] The parallel-plate chamber measurements were therefore used to assess the accuracy of the shape of the depth dose curves measured with the diode detectors, including the peak-to-plateau ratio and width of the Bragg peak. These measurements were done with a Roos (PTW-Freiburg model N34001) parallel-plate chamber, a Markus (PTW-Freiburg) parallel-plate chamber, and the PTW diode. In this case, the water tank was 150 mm from the exit window. The relatively large surface area of the parallel-plate chambers made the positioning of these chambers less accurate than for the diodes. The detector was positioned with its surface coincident with the Mylar wall to set zero depth on the scanner as follows. Square water equivalent slabs (CIRS Plastic Water) totaling 32 mm in thickness were placed upstream of the water tank within a few centimeters of the Mylar wall. With the detector positioned within millimeters of the Mylar wall, this placed the detector in the high dose gradient on the proximal side of the Bragg peak. The detector was moved in 0.1 mm increments toward the wall until the rate of change of the dose with depth dropped off, signaling the absence of water between the detector surface and Mylar wall. The detector was then moved back 0.05 mm and this was the zero position. The distance of the effective point of measurement from the detector surface was 1.18 mm water equivalent for the Roos chamber (1.18 mg/cm^2 acrylic, manufacturer specification) and 1.0 mm for the Markus (manufacturer specification). With this positioning method, the depth of the sensitive volume of the diode had an uncertainty of approximately 0.3 mm. The larger areas of the ion chambers made it difficult to align the detector surface parallel to the Mylar wall and this led to a larger uncertainty in the depth. The accuracy of this positioning method for the ion chambers was assessed by comparing the position of the distal edge of the Bragg peak with the diode measurements.

Raw beam measurements were made with the Roos and Markus chambers at a nominal 300 pA beam current and the diodes at 25–50 pA. To demonstrate that the dose rate was sufficiently low that ion recombination could be neglected, the measurements were repeated in the Bragg peak and near the surface at reduced (half or a third) beam current. The measured peak-to-plateau ratio was found to be independent of beam current within the repeatability of the measurements of 1.4%, one standard deviation, for both the ion chamber and diode measurements. The same or lower dose rate was used for measuring depth dose curves on the eye treatment beam line.

Profiles were measured to determine beam characteristics including field size and symmetry. These do not serve as benchmarks as information on the angular distribution of the source is lacking, the fields are asymmetric over the 6 cm diameter final collimator (having no clinical impact for the much smaller fields used to treat eyes), and scatter from the beam line contributes to the profiles. Scatter benchmarks would be better measured with narrow beams incident on thin foils, as done for electron beams.[30] Radiochromic film has proven to be useful in measuring dose distributions in proton beams.[31,32] The flatness and symmetry of the beam was measured with radiochromic film (Gafchromic EBT3) for both the raw beam line and eye treatment beam line. Beam divergence was measured with radiochromic films placed 300 mm apart in the raw beam line. The measurements were used to determine whether asymmetry could be ignored in the simulation for both beam lines and whether beam divergence could be ignored in the case of the eye treatment beam line.

2.C. Simulation

Monte Carlo simulation was done using TOPAS (Ref. 6) beta version 1.0-b9 with the GEANT4 toolkit[33] version 9.6.p2 with the physics option StandardEMPhysics_option 3. The beam line geometries as simulated are given in the Appendix. The

simulations included all of the components that could have a significant influence on the depth dose curve, outside of experimental uncertainty. The aluminum coating on the mirror in the eye treatment beam line was not included. The default range cut of 0.05 mm was used for most of the geometry components in the simulation. A 0.02 mm range cut was used for the beam plug (C2 in Fig. 1), giving the best match to the benchmark measurements for the thicker foil (see Sec. 3).

The energy of the proton source for both beam lines was 67.5 MeV. For simulation of the raw beam line, the peak in the source energy distribution had a Gaussian spread of width determined to match the slope of the distal edge of the Bragg peak measured with the thinner Ta foil. The peak width was constrained to be no greater than 0.4 MeV, the width measured with CsI. The raw beam line source was simulated as a uniform 5×10 mm oval spot normally incident on the foil. The simulation was insensitive to spot size at the foil, with negligible difference in the Bragg curve simulated with zero spot size and the oval spot as shown later.

The source for the eye treatment beam line was a constant fluence 60 mm diameter circle normally incident on the wire chamber. There was no need to simulate the beam line up to the wire chamber since without a scattering foil, both energy degradation (with only vacuum up to the wire chamber) and collimator scatter (with no foil to scatter the proton beam into the beam tubes) were negligible. There was no beam focusing in the eye treatment beam line, resulting in a substantially broader peak in the energy distribution, as evidenced by the breadth of the Bragg peak compared to that in the raw beam. The peak FWHM was chosen to match the width of the Bragg peak measured for the eye treatment beam line. This same FWHM was used in simulating the SOBP.

The water tank was simulated as a 0.25 mm thick Mylar plate followed by 0.05 mm thick plates of water down to a depth of 50 mm. Dose to water and dose to Bragg–Gray cavities of Si and air was scored in the water plates along the central axis of the beam in 10 mm diameter $\times$ 0.05 mm thick voxels. The calculation of dose to a Bragg–Gray cavity provides the SPR data needed to convert the measured ionization in a detector sensitive volume composed of nonwater material (Si or air) to dose to water at the position of the detector sensitive volume.[3,24] This gives a relative dose assuming the perturbation factor, W_Si-value and W_air-value are independent of energy (depth). Sufficient particles were simulated to reach a calculation precision of 0.5% or better in voxels with values larger than 10% of the maximum dose.

3. RESULTS AND DISCUSSION

3.A. Bragg curve simulation and measurement

Simulated raw beam line depth dose and depth ionization curves are shown in Fig. 4. The SPR of water-to-silicon and water-to-air calculated with Monte Carlo simulation is shown in the inset. The water-to-air SPR, varies by 1.0% from 10 mm to the Bragg peak as calculated with GAMOS for 70 MeV protons with depth shifted to match R_{80}, the 80% depth at the distal side of the Bragg peak from the TOPAS 67.5 MeV Bragg curve. The

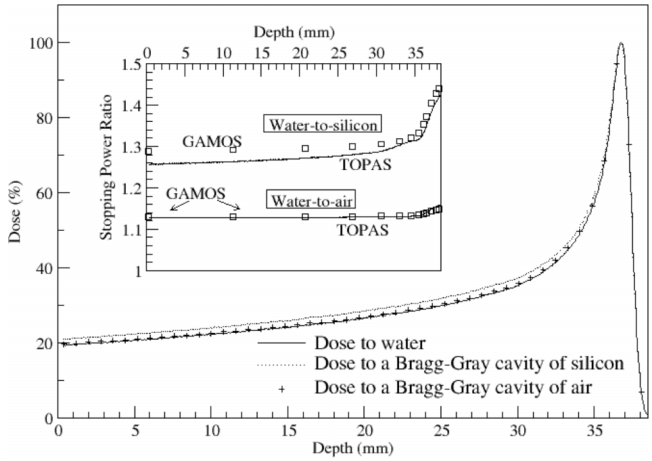

FIG. 4. Percent depth dose curves including dose to water and dose to a Bragg–Gray cavity in water, simulated with TOPAS for a 67.5 MeV proton beam with a 0.4 MeV FWHM peak transported through the raw beam line and incident on the thinner Ta foil. Dose to water compared to dose to Bragg–Gray cavities of silicon and air in water from the same simulation, normalized at the Bragg peak to show the effect of the SPR on the peak-to-plateau ratio. Inset shows the SPR calculated from these curves as the ratio of the water dose to the Bragg–Gray cavity dose (solid lines), compared to the SPR calculated with GAMOS (squares).

variation calculated by TOPAS over this depth range was 1.5%. With R_{80}, shifted to match the TOPAS result, the water-to-silicon SPR from 10 mm depth to the Bragg peak varies by 7.1% as calculated by GAMOS, 7.9% as calculated by TOPAS, a 0.8% difference in the SPR correction for the diode measurements. Given these small differences, the published GAMOS results for 70 MeV protons were used in this study to correct the depth ionization curves measured for the Bragg peak to dose to a Bragg–Gray cavity of water. Thus, there is a 0.5% difference in the correction of the parallel-plate chamber measurements to dose to water and a 0.8% difference in the correction of the diode measurements to dose to water. The difference between the simulations is attributed to the more complicated geometry and source in the benchmark setup simulated with TOPAS, including the contribution of lower energy protons scattered from the material upstream of the water and the width of the peak in the energy distribution.

The GAMOS and TOPAS simulations both used an I-value for water of 78 eV. A 3 eV decrease in this I-value results in a 0.6% increase in the calculated stopping power for water in the region upstream of the Bragg peak.[29] Published I-values for water vary with recently used values ranging from 73 to 82 eV.[4,34]

The use of diode detectors to measure the Bragg curve benchmarks was validated in this study with a comparison of the diode measurements to ion chamber measurements, with ionization corrected to dose to water for both the diode detector and ion chamber measurements using published SPRs. Depth dose curves for the raw beam measured with the PTW diode and Markus and Roos parallel-plate chambers with the water tank 150 mm from the exit window are shown in Fig. 5. An analytical approximation of the depth dose curve[35] was fit to the measured curves in the region of the Bragg peak

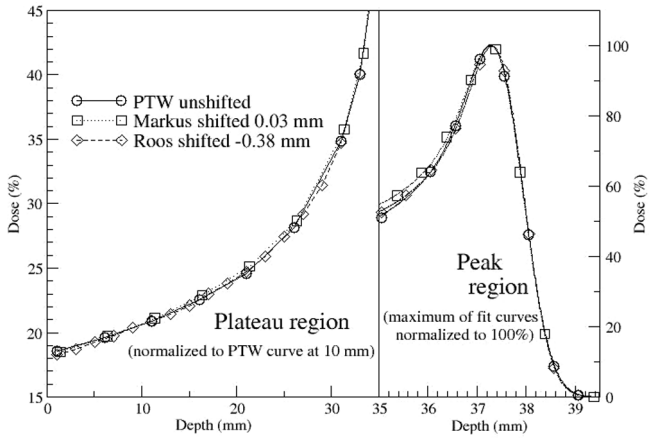

FIG. 5. Bragg curves measured with PTW diode and Markus and Roos parallel-plate chambers (points) on the raw beam line to establish the accuracy of the diode for benchmark measurements of the shape of the Bragg curve. The dose scale is magnified on the left hand side plot to better show the plateau region, with points joined by straight lines. The depth scale is magnified on the right hand side plot to better show the peak region. The ion chamber measurements were shifted to match the diode measurement at the distal edge of the Bragg peak. The ion chamber measurements on the left are normalized at 10 mm depth to match the diode measurement at that depth and the curves on the right are normalized to 100% at the Bragg peak, using the analytical function fit to the points. Depth accuracy of the diode was improved in subsequent measurements.

and normalized to 100% at the Bragg peak to more accurately determine the peak-to-plateau ratio.

The uncertainty in the peak-to-plateau ratio was 2% for the ion chambers and 4% for the diode. This includes a 3% uncertainty in the normalization due to the 0.5 mm step size in the measurements for this set of data, 1.4% repeatability, a 2% uncertainty in the SPR for the diode, and a 2% uncertainty due to drift in the diode reading. A linear correction with charge collected was applied to the diode readings since the reading at 10 mm depth drifted 3.5% over the course of the measurements. Relative uncertainties were added in quadrature.

The results for the diode agree with the results for the parallel-plate chambers within experimental uncertainty. The peak-to-plateau ratio measured with the diode was $(6 \pm 5)\%$ higher than measured with the Markus chamber, $(4 \pm 5)\%$ for the Roos chamber. The difference in the position of the distal edge of the Bragg peak was 0.03 mm for the Markus chamber and 0.38 mm for the Roos chamber. The agreement validates the use of diodes within the experimental uncertainty to measure the benchmark depth dose curves, including all factors that may contribute to a difference in the diode and ion chamber measurements.[27,28,36] The water equivalent depth of the sensitive volume of the diode detectors in water was known with higher accuracy than the depth of the sensitive volume of the ion chambers in the water tank. Diodes were chosen for measurement of the Bragg curves to take advantage of the more accurate depth measurement. The Roos position was at the edge of the 0.3 mm uncertainty in the diode positioning (the diode positioning was more accurate for the benchmark measurement). The larger surface area of the Roos chamber made it more difficult to align to the Mylar wall of the water tank, resulting in a larger positioning uncertainty.

Previous studies with p-type silicon detectors such as the diodes employed in this study applied no SPR correction to measure dose to air to compare to ion chamber measurements.[27] However, in the current study, the application of the water-to-air SPR rather than the water-to-silicon SPR to the depth dose curves measured with diodes would lead to a 7% difference in the peak-to-plateau ratio compared with the ion chamber measurements. Thus, the water-to-silicon SPR was used to correct the diode measurements to dose to water as done in more recent studies.[28,37]

3.B. Bragg curve experimental benchmark

Bragg curves measured in the raw beam line with the PTW and EFD diodes for two thicknesses of Ta foil with the water tank 300 mm from the exit window are tabulated in the Appendix. A linear correction with charge collected was applied to the PTW diode reading since the reading at 5 mm depth drifted 1.8% over the course of the measurements. For these measurements, the depth of the surface of the diode was determined using the distance gauge with an accuracy of 0.1 mm. The Bragg curves were shifted to account for the Mylar window on the water tank and the water equivalent depth of the sensitive volume of the detector. The distal edge of the Bragg peak for the thinner foil is 0.27 $\pm$0.21 mm deeper for the EFD diode than for the PTW diode, that is, within 1.3 standard deviations of the experimental uncertainty.

The field was sufficiently wide (8.88 cm diameter collimator) that the depth of the distal edge of the Bragg peak was insensitive to field size. Flatness and symmetry of the raw beam were measured with radiochromic film at the water tank. The dose to the film dropped an average of 10% at 30 mm off axis. Asymmetry in the beam gave a ratio of dose at 30 mm off axis on either sides of the field of 1.03 vertically and 1.47 horizontally. The beam divergence measured for the raw beam was 0.3° at the edge of the 80 mm diameter field at the water tank. The assumptions of radial symmetry on the peak-to-plateau ratio and depth penetration were assessed with Monte Carlo simulation for the raw beam line. The assumptions of radial symmetry and no beam divergence with a perfectly flat beam were assessed with Monte Carlo simulation for the eye treatment beam line. The simulated depth dose curves with ideal sources compared within statistical precision to those simulated using the flatness, symmetry, and beam divergence measured on the raw beam. The carbon collimator also had negligible impact on the simulation.

The measured benchmark is shown in Fig. 6. The 80% dose at the distal side of the Bragg peak for the thinner foil was at 37.35 ± 0.15 mm for the PTW diode and 37.58 ± 0.15 mm for the EFD diode, an average of 37.47 ± 0.11 mm. The 80% dose for the thicker foil was at 35.08 ± 0.15 mm. The peak-to-plateau ratio was calculated as the ratio of the dose at the Bragg peak to that at 10 mm depth. For 0.1016 mm Ta, this was 4.39 ± 0.18 as measured by the PTW diode and 4.26 ± 0.17 as measured by the EFD diode, the separate measurements agreeing within experimental uncertainty. The average peak-to-plateau ratio measured for the thin foil was 4.33 ± 0.12. For

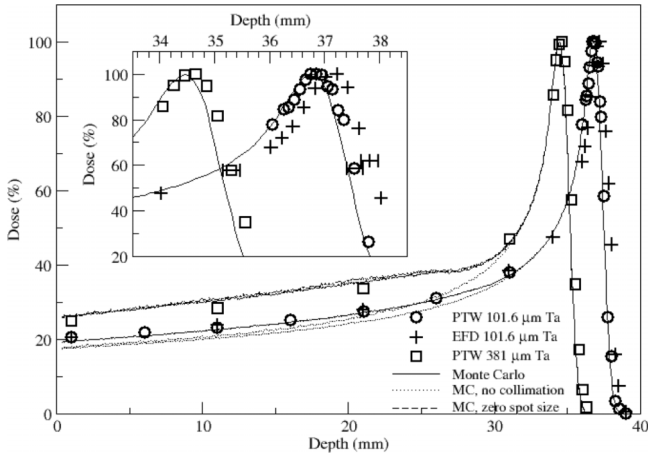

FIG. 6. The raw beam Bragg curves measured with PTW and EFD Si diodes (points). The inset is a magnified view of the Bragg peak, with depth accuracy of ±0.15 mm shown on the points closest to 50% of the maximum dose. Monte Carlo Bragg curves (lines) for 67.5, 0.4 MeV FWHM, 5×10 mm^2 protons simulated with TOPAS. Additional simulations are shown without collimation for both foils (dotted lines) and for zero spot size for the thicker foil (dashed line).

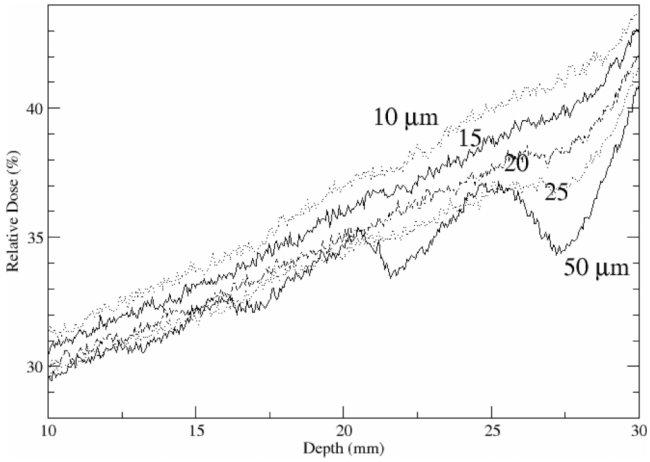

FIG. 7. The effect of changing the production cut in the beam plug on the simulation of the raw beam Bragg curve. Normalized to 100% at the Bragg peak to show the effect of the production cut on the peak-to-plateau ratio.

0.381 mm Ta, the ratio measured with the PTW diode was 3.57 ± 0.14.

The Monte Carlo simulation results are also shown in Fig. 6. Results of additional simulations shown in the figure demonstrate the importance of including the collimation in the simulation and the insensitivity of the result to spot size. A peak FWHM of 0.4 MeV in the simulation, equal to the upper limit of the FWHM measured with CsI, gave a good match to the shape of the Bragg peak. The distal edge of the simulated Bragg peak is proximal to the measurements for both foils by 1–2 standard deviations experimental uncertainty: 0.15 ± 0.15 mm for the thin foil PTW measurement, 0.39 ± 0.15 mm for the thin foil EFD measurement, and 0.17 ± 0.15 mm for the thicker foil PTW measurement. The I-value of water proved sufficient for calculating the depth penetration, and thus the stopping powers used in the Monte Carlo simulation, within 0.4%–1%. Given a 3 eV increase in the I-value results in a 0.6% decrease in stopping power of protons in water,[29] suggesting an I-value of water of 80–83 eV.

The peak-to-plateau ratio for the thicker foil was sensitive to the range cut (Fig. 7). In this case, the default range cut of 0.05 mm resulted in nonphysical undulations in the plateau region. The undulations are due to primary protons deflected from the beam plug after (nonphysically) losing a minimum amount of energy, dependent on the range cut (seen in the simulated primary proton spectrum at the water surface as equally spaced peaks of diminishing energy). The other collimating components were much shorter than the beam plug and consequently contributed relatively few deflected protons to dose in the water phantom (also seen in the simulation). A lower range cut in the beam plug reduced the amplitude of the undulations. A 0.02 mm range cut gave a reasonable match to the measured peak-to-plateau ratio for the thicker foil (3% lower than measurement at 10 mm depth as seen in Fig. 7) with only a minimal artifact (1.5% at 27 mm depth). Bragg curves measured with radiochromic film (Gafchromic EBT3) for the two foils (results not shown) were smooth, further demonstrating that the undulations seen in the simulations with the higher range cut were not physical. A 0.02 mm range cut was therefore used for the beam plug for simulations with both the thinner and thicker foil. The default 0.05 mm range cut was used for all other geometry components.

The simulated peak-to-plateau ratio for the 0.1016 mm Ta foil was 4.47 ± 0.02 (statistical uncertainty), within one standard deviation of the measured value for both diode detectors. The simulated ratio for the 0.381 mm foil was 3.31 ± 0.02, just within two standard deviations of measurement. Note that it is essential to simulate the collimating components. When they are left out of the simulation, the peak-to-plateau ratio increases by a factor of 1.11 for the thinner foil and 1.45 for the thicker foil (Fig. 6). Unfortunately, the components are under vacuum and were inaccessible for direct measurement of their geometry. Thus, the proton Bragg curve measured for the thinner foil provided a more accurate benchmark.

3.C. Eye treatment beam line Bragg curve and SOBP

Depth dose curves were measured in the eye treatment beam line for a pristine Bragg peak and a SOBP. The pristine Bragg peak was produced with the range modulator wheel (RMW), shown in Fig. 1, removed. A rotating RMW (P in Fig. 1) was placed in the beam line to spread out the Bragg peak, producing a SOBP with a nominal 20 mm width. In this case, a nominal 10 mm of water was pumped into the water column (H2O in Fig. 1). Results are tabulated in the Appendix. The uncertainties of beam energy and relative ionization for the Bragg peak measurement are the same as those for the raw beam with an added uncertainty of 1–3 mm for the thickness of water in the water column (H2O in Fig. 2). There was potential for residual water left in the water column with the piston closed. The water column is essential for treatment,

making it impractical to remove for direct measurement. The SOBP measurement has additional uncertainties for the mass thicknesses and angles subtended by the plates in the RMW blades and the water-to-silicon SPR. A single plate thickness was used in the simulation, set to the value, within the uncertainty of the measured variability of the thickness, to match the width of the measured SOBP.

The distal edge of the Bragg curve was not as steep in the simulation when using the same energy distribution of the incident proton beam used in the raw beam simulation. A broader peak for the eye treatment beam line is plausible, without the focusing magnets. An increased FWHM of 1.3 MeV gave the best match within 0.1 MeV to the distal slope and peak-to-plateau ratio. A 0.1 MeV change in the peak FWHM resulted in a 2% change in the peak-to-plateau ratio.

The amount of water in the water column could not be determined with submillimeter accuracy by direct observation. In the simulations, the amount of water in the water column was increased to match the measured depth dose curves at 50% of the maximum dose on the distal side to better than 0.1 mm. The amount of water used (the water column component of Table III in the Appendix) was 2.24 mm for the Bragg peak and 11.30 mm for the SOBP. In this case (Fig. 8), with the dose normalized to 100% at the peak, the simulated Bragg peak agrees with measurement within 1%/0.1 mm; that is, the least restrictive of 1% in dose (taking the difference in dose) and 0.1 mm in distance to agreement. The accuracy of the measurements for validation of simulation is 2 mm in depth (limited by the uncertainty in the amount of water in the water column) and 4% in the peak-to-plateau ratio (as for the Bragg curve benchmark measurement).

The SOBP was simulated using the same 1.3 MeV peak FWHM used in simulating the Bragg peak. In this case, the tail end of the simulated SOBP is 4% higher than measurement (Fig. 8). If this region is omitted, simulation agrees with measurement within 2%/0.1 mm. The agreement over the full SOBP was improved to 2%/0.1 mm by increasing the angle subtended by the first plate in the four sectors of the RMW by 1°. Such adjustments are within experimental uncertainty, giving sufficient freedom to adjust the RMW dimensions in the simulation to achieve an arbitrarily good match with measurement. Thus, the 3%/0.1 mm agreement with the measured SOBP is within experimental uncertainty.

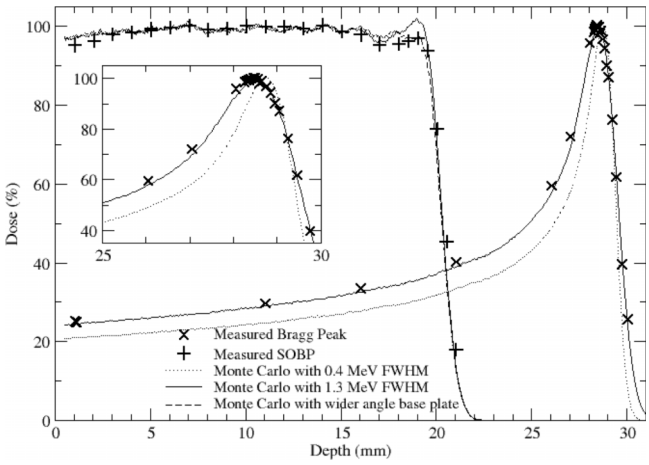

FIG. 8. Proton depth ionization curves for eye treatment beam line measured with the PTW diode: Bragg peak and 20 mm SOBP with a nominal 10 mm water column. Curves are normalized to 100% at the Bragg peak to show the effect of the peak width on the peak-to-plateau ratio. Simulations had a thicker water column than the nominal thickness. Bragg curve simulated with different widths of the peak in the energy distribution. SOBP simulated with the measured angles subtended by the RMW blades and a 1° wider angle used for the base plate (both 1.3 MeV peak FWHM).

4. CONCLUSIONS

Benchmark Bragg curves were measured for a 67.5 ± 0.1 MeV proton beam incident on two different thicknesses of Ta foil with 0.15 mm accuracy in depth and 4% accuracy in the peak-to-plateau ratio. The experimental uncertainties account for the mean energy and spread of the incident proton beam and uncertainty in the beam-line geometry. The measurements provide new experimental benchmarks with source energy and depth accuracy that to our knowledge exceeds that of published data. Monte Carlo simulations matched the measured peak-to-plateau ratio within one standard deviation of the experimental uncertainty for the thinner foil and two standard deviations for the thicker foil. The depth penetration fell short of measurement by $0.7\% \pm 0.3\%$ for the thinner foil and $0.5\% \pm 0.4\%$ the thicker foil. This suggests an I-value of water of 80–83 eV on the high end of values reported in the literature.

The Bragg curve and SOBP measured on the Crocker Lab eye treatment beam line are the most accurate measurements and most highly constrained simulations of this beam line published to date. Given the uncertainty in RMW geometry and the thickness of material, the beam passes through in the beam line, the measured Bragg curve, and SOBP serve for validation of Monte Carlo simulation of beams from a clinical beam line, rather than a benchmark.

ACKNOWLEDGMENTS

This work was partially supported by the U.S. National Institutes of Health/National Cancer Institute (NIH/NCI) under No. R01 CA140735. The authors are grateful to Randy Kemmler and Paul Wakabayashi of Crocker Lab for their able technical assistance, Vladimir Ivanchenko of CERN and EMSU Lomonosov Moscow State University for helpful discussions on GEANT4 simulation, and Melanie Regan and Youngho Seo of UCSF for the microCT scans they took of the diodes.

APPENDIX: SIMULATION DETAILS

1. Bragg curve experimental benchmark

A 67.5 MeV proton beam from the cyclotron with a peak FWHM of 0.4 MeV and a uniform oval spot of 5×10 mm

TABLE I. Geometry of raw beam line as specified in the simulation. The term "thick" is used to specify the dimension along the beam axis. The intervening material upstream of the exit window is vacuum and downstream of the exit window is air of 1.20 mg/cm^2, composed of 0.012% C, 75.53% N, 23.18% O, and 1.28% Ar. The evacuated box has holes larger than the inner diameter of the collimators on either sides. Materials are pure unless otherwise stated. The composition of stainless steel in the simulation was 0.15% C, 1% Si, 0.045% P, 0.03% S, 19% Cr, 2% Mg, 67.8% Fe, and 10% Ni.

Component	Subcomponent	Geometry	Material	Position of upstream surface (mm)
Scattering foil	Plate	101.6 mm radius, 0.1016 mm or 0.381 mm thick	Ta, 16.65 g/cm^3	0
Collimator	Hollow cylinder	4.76 mm inner radius, 51 mm outer radius, 25.4 mm thick	Carbon, 1.867 g/cm^3	30
Beam plug	Hollow cylinder	63.5 mm inner radius, 70 mm outer radius, 3000 mm thick	Stainless steel, 8.027 g/cm^3	710
Beam pipe	Hollow cylinder	50.8 mm inner radius, 70 mm outer radius, 330 mm thick	Al, 2.699 g/cm^3	3710
Collimator	Hollow cylinder	34.9 mm Inner radius, 70 mm outer radius, 40 mm thick	Stainless steel, 8.027 g/cm^3	4040
Box	Plate with circular hole in center	Wall with 50 mm radius circle, 280 mm wide square, 10 mm thick	Al, 2.699 g/cm^3	4080
	Square box	Wall 267 mm wide inside, 280 mm wide outside, 490 mm thick	Al, 2.699 g/cm^3	4090
	Plate with circular hole in center	Wall with 50 mm radius circle, 280 mm wide square, 10 mm thick	Al, 2.699 g/cm^3	4580
SEM (in the box)	3 plates (Al foils)	Each foil 101.6 mm radius, 6.35 μm thick, 25.4 mm between foils	Al, 2.699 g/cm^3	4140, 4165.4, 4190.8
Collimator	Hollow cylinder	Wall with 44.4 mm inner and 60 mm outer radius, 50 mm thick	Stainless steel, 8.027 g/cm^3	4590
Exit window	Plate	0.127 mm thick	Kapton, 1.42 g/cm^3	4640
Water tank	Plate	0.25 mm thick	Mylar, 1.40 g/cm^3	4940
	Plate	50 mm thick	H_2O, 0.998 g/cm^3	4940.25

TABLE II. Bragg curve benchmarks measured in raw beam line with diodes, with a depth uncertainty of 0.15 mm, and peak-to-plateau ratio uncertainty of 4%. Depth is that of sensitive volume of detector in water accounting for water equivalent thickness of detector material. Water surface is at 0.35 mm depth (mass thickness of Mylar window).

PTW diode, 0.1016 mm Ta		PTW diode, 0.381 mm Ta		EFD diode, 0.1016 mm Ta	
Depth (mm)	Relative dose (%)	Depth (mm)	Relative dose (%)	Depth (mm)	Relative dose (%)
1.06	20.4	1.06	24.9	1.03	20.5
6.06	21.7	11.06	28.3	11.03	23.8
11.06	23.1	21.06	33.6	21.03	28.0
16.06	25.0	31.06	46.9	31.03	38.4
21.06	27.4	34.06	85.6	34.03	47.5
26.06	31.0	34.26	95.0	36.03	67.8
31.06	37.9	34.46	99.2	36.23	71.9
36.06	77.7	34.66	100.0	36.43	76.8
36.26	84.3	34.86	94.7	36.63	85.1
36.36	85.3	35.06	81.5	36.83	93.5
36.46	88.7	35.31	57.5	37.03	98.8
36.56	93.0	35.56	34.8	37.23	100.0
36.66	97.5	35.81	17.2	37.43	94.0
36.76	100.0	36.06	6.5	37.63	75.9
36.86	100.0	36.31	1.7	37.83	61.9
36.96	99.4			38.03	45.5
37.06	94.3			38.28	15.9
37.16	93.2			38.53	7.4
37.26	83.8			39.03	0.4
37.36	79.7				
37.56	58.4				
37.81	25.9				
38.06	15.3				
38.31	3.2				
38.56	1.2				
39.06	0.04				

TABLE III. Geometry of eye treatment beam line as specified in the simulation. The term thick is used to specify the dimension along the beam axis. The intervening material upstream of the exit window is vacuum, downstream of the exit window is air (see Table I caption). The ion chamber has 3 gold-plated Kapton plates enclosing 2 gas-filled regions. The Mylar window of the water phantom was positioned 50 mm from the downstream end of the patient assembly. Acrylic was simulated as 8% H, 60% C, and 32% O (G4_plexiglass). Brass was simulated as 70% Cu, 30% Zn.

Component	Subcomponent	Geometry	Material	Position of Upstream Surface (mm)
Wire chamber	Plate	150×150 mm^2, 0.127 mm thick	Kapton, 1.42 g/cm^3	0
	Two layers of 72 wires	Wires of 29 μm radius, 320 mm length, 2 mm spacing, 10 mm between layers	Brass, 8.55 g/cm^3, with N_2 gas, 0.001 251 g/cm^3	12.25
	Plate	150×150 mm^2, 0.127 mm thick	Kapton, 1.42 g/cm^3	34.5
SEM	5 plates (Al foils)	Each foil 80 mm radius, 6.35 μm thick, 14 mm between foils	Al, 2.699 g/cm^3	40, 54, 68, 82, 96
Exit window	Plate	110 mm radius, 25 μm thick	Mylar, 1.40 g/cm^3	100
Wire chamber	Plate	150×150 mm^2, 0.127 mm thick	Kapton, 1.42 g/cm^3	164
	Two layers, 72 wires each layer	Wires of 29 μm radius, 320 mm length, 2 mm spacing, 10 mm between layers	Brass, 8.55 g/cm^3, with N_2 gas, 0.001 251 g/cm^3	176.25
	Plate	150×150 mm^2, 0.127 mm thick	Kapton, 1.42 g/cm^3	198.5
Collimator	Hollow cylinder	26 mm thick, 25 mm inner radius, 150 mm outer radius	Brass, 8.55 g/cm^3	248
Ion chamber	Plate	0.254 mm thick, 200 mm radius	Kapton, 1.42 g/cm^3	324
	Plate	10^{-7} mm thick, 200 mm radius	Au, 19.3 g/cm^3	324.254
	Plate	48 mm thick, 200 mm radius	N_2, 0.001 251 g/cm^3	324.254 + 10^{-7}
	Plate	10^{-7} mm thick, 200 mm radius	Au, 19.3 g/cm^3	348
	Plate	0.254 mm thick, 200 mm radius	Kapton, 1.42 g/cm^3	348 + 10^{-7}
	Plate	10^{-7} mm thick, 200 mm radius	Au, 19.3 g/cm^3	348.254 + 10^{-7}
	Plate	48 mm thick, 200 mm radius	N_2, 0.00 1251 g/cm^3	348.254 + 2 ×10^{-7}
	Plate	10^{-7} mm thick, 200 mm radius	Au, 19.3 g/cm^3	372
	Plate	0.254 mm thick, 200 mm radius	Kapton, 1.42 g/cm^3	372 + 10^{-7}
RMW	Stacked plates	1.54 mm thick plates with vertex and angle given in Table IV	Acrylic, 1.19 g/cm^3	545
Collimator	Hollow cylinder	25 mm thick, 25 mm inner radius, 150 mm outer radius	Brass, 8.55 g/cm^3	665
Water column	Plate	1.27 mm Thick	Acrylic, 1.19 g/cm^3	1193.73 - t_{water}
	Plate	t_{water} thick (2.24 mm for Bragg peak, 11.3 mm for SOBP)	H_2O, 0.998 g/cm^3	1195 - t_{water}
	Plate	1.27 mm thick	Acrylic, 1.19 g/cm^3	1195
Collimator	Hollow cylinder	25 mm thick, 25 mm inner radius, 150 mm outer radius	Brass, 8.55 g/cm^3	1196.27
Ion chamber	See above			1603
Mirror	Plate at 45°	0.13 mm thick (0.18 mm along beam axis), 35 mm radius	Mylar, 1.40 g/cm^3 (coated with Al)	1677.38
Patient shield	Hollow cylinder	16.5 mm thick, 25 mm inner radius, 305 mm outer radius	Al, 2.699 g/cm^3	1728
Patient assembly	Hollow cylinder	218 mm thick, 34.8 mm inner radius, 50.0 mm outer radius	Brass, 8.55 g/cm^3	2229.5
Water tank	Plate	0.25 mm thick	Mylar, 1.40 g/cm^3	2280
	Plate	50 mm thick	H_2O, 0.998 g/cm^3	2280.25

was normally incident on the components of the raw beam line (Fig. 1) listed in Table I. Sufficient details of the geometry and material are given for the purpose of simulation. Simplifications were made without a significant loss of accuracy in the simulation compared to experimental uncertainty. Protons impinging on the raw beam line traversed one of two thicknesses of Ta scattering foil followed by a wire chamber, secondary emission monitor (SEM) and exit window. The low mass per unit area of material traversed by the beam between the cyclotron and water phantom leads to a more

TABLE IV. Measured position of vertex of each of the 11 pie-shaped 20 mm SOBP RMW plates relative to the center of rotation of RMW in each of the 4 sectors and angle subtended by each plate from the vertex.

	Sector 1			Sector 2			Sector 3			Sector 4		
Plate	Vertex (mm)		Angle (deg)	Vertex (mm)		Angle (deg)	Vertex (mm)		Angle (deg)	Vertex (mm)		Angle (deg)
1	−2.2	−1.5	74.8	−2.2	−2.0	75.0	−2.1	−1.7	75.0	−2.1	−1.9	75.0
2	−2.2	−1.5	69.1	−1.7	−2.6	69.1	−2.1	−1.7	68.7	−1.8	−1.4	68.7
3	−2.2	−1.5	62.8	−1.7	−2.6	62.3	−2.1	−1.7	61.7	−1.1	−1.4	61.9
4	−2.2	−1.5	56.6	−1.7	−2.6	56.5	−1.5	−0.9	56.1	−1.1	−1.4	55.5
5	−2.2	−1.5	50.6	−1.7	−2.6	50.5	−1.5	−0.9	50.4	−1.1	−1.4	50.5
6	−2.2	−1.5	44.7	−1.5	−2.9	44.8	−1.5	−0.9	44.1	−1.1	−1.4	43.9
7	−2.2	−1.5	38.5	−0.6	−3.3	39.1	−1.5	−0.9	38.1	−1.1	−0.3	38.6
8	−2.2	−1.5	31.8	−0.6	−3.3	31.9	−1.5	−0.9	31.0	−1.1	−0.3	31.2
9	−2.2	−1.5	25.1	−0.5	−0.9	24.6	−1.5	−0.9	24.6	−1.1	−0.3	24.9
10	−2.2	−1.5	17.3	−0.5	−0.9	17.1	1.0	0.0	17.7	−1.1	−1.3	17.3
11	−2.2	−1.5	9.4	−0.5	−0.9	9.2	1.0	0.0	9.6	−1.1	2.3	9.4

accurate benchmark of depth penetration in water as the simulation is not sensitive to the small energy loss in the material. The density of Kapton varies from 1.4 to 1.7 g/cm^3 (manufacturer specification). This can be considered a negligible uncertainty.

The benchmark Bragg curves, measured with diodes, with the water-to-silicon SPR applied (Fig. 6), are shown in Table II.

2. Eye treatment beam line Bragg curve and SOBP

A 67.5 MeV proton beam with a peak FWHM of 1.3 MeV from the cyclotron was normally incident, with a circular spot 60 mm in diameter, on the components of the eye treatment beam line (Fig. 2) listed in Table III. A RMW was used to give a 20 mm SOBP and was used with a nominal 10 mm of water pumped into the water column. A single plate thickness was used in the simulation for the RMW, set to the value, within the uncertainty of the measured variability of the thickness, to match the width of the measured SOBP.

The measured dimensions of the RMW are shown in Table IV. The RMW (Fig. 9) is divided into 4 roughly equivalent sectors each covering 90° of the rotation. Each sector consists of a stack of 11 pie-shaped plates of roughly equal thickness. The center of rotation of the RMW is the center of the brass ring. The position of the vertices relative to the center of rotation was measured within 0.4 mm. The angle subtended by each plate from the vertex was measured within 1°.

The Bragg curve and SOBP measured on the eye treatment beam line with diodes, with the water-to-silicon SPR applied (Fig. 8), are shown in Table V.

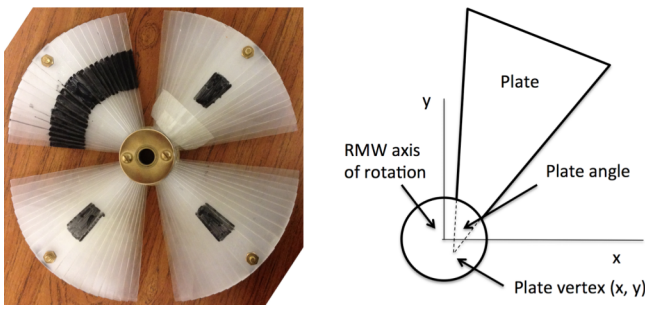

FIG. 9. Photograph of range modulator wheel with schematic of a plate in one of the sectors.

TABLE V. Depth dose curves measured on the eye treatment beam line with the PTW diode with a depth accuracy of 0.15 mm: Bragg peak and 20 mm SOBP with 10 mm water column. Depth is that of sensitive volume of detector in water accounting for water equivalent thickness of detector material. Water surface is at 0.25 mm depth (thickness of Mylar window).

Bragg curve		Spread out Bragg peak	
Depth (mm)	Relative dose (%)	Depth (mm)	Relative dose (%)
1.06	25.0	1.06	95.1
1.11	24.7	2.06	96.1
1.16	24.7	3.06	97.9
11.06	29.5	4.06	98.4
16.06	33.4	5.06	98.9
21.06	40.3	5.06	99.4
26.06	59.6	6.06	99.6
27.06	72.2	7.06	100.1
28.06	95.5	8.06	99
28.26	99.0	9.06	99.4
28.31	98.9	10.06	100
28.36	99.7	11.06	99.8
28.41	98.2	12.06	99.9
28.46	100.0	13.06	99.3
28.51	99.7	14.06	100.2
28.56	99.6	15.06	98.6
28.61	97.9	16.06	97.8
28.66	98.7	17.06	95.3
28.76	96.5	18.06	95.4
28.86	93.4	18.56	96.2
28.96	89.8	19.06	96.9
29.06	86.1	19.56	93.7
29.26	75.4	20.06	74
29.46	60.4	20.56	45.2
29.76	38.9	21.06	17.8
30.06	25.3		

[a]Author to whom correspondence should be addressed. Electronic mail: bfaddegon@radonc.ucsf.edu

[1]T. Bortfeld and R. Jeraj, "The physical basis and future of radiation therapy," Br. J. Radiol. **84**, 485–498 (2011).

[2]See http://www.ptcog.ch for the Particle Therapy Co-Operative Group (PTCOG).

[3]I. J. Chetty, B. Curran, J. E. Cygler, J. J. DeMarco, G. Ezzell, B. A. Faddegon, I. Kawrakow, P. J. Keall, H. Liu, C. Ma, D. W. O. Rogers, J. Seuntjens, D. Sheikh-Bagheri, and J. V. Siebers, "Report of the AAPM Task Group No. 105: Issues associated with clinical implementation of Monte Carlo-based photon and electron external beam treatment planning," Med. Phys. **34**, 4818–4853 (2007).

[4]H. Paganetti, "Range uncertainties in proton therapy and the role of Monte Carlo simulations," Phys. Med. Biol. **57**, R99–R117 (2012).

[5]M. Testa, J. Schümann, H.-M. Lu, J. Shin, B. Faddegon, J. Perl, and H. Paganetti, "Experimental validation of the TOPAS Monte Carlo system for passive scattering proton therapy," Med. Phys. **40**(12), 121719 (16pp.) (2013).

[6]J. Perl, J. Shin, J. Schümann, B. Faddegon, and H. Paganetti, "TOPAS–An innovative proton Monte Carlo platform for research and clinical applications," Med. Phys. **39**, 6818–6837 (2012).

[7]X. Jia, J. Schumann, H. Paganetti, and S. B. Jiang, "GPU-based fast Monte Carlo dose calculation for proton therapy," Phys. Med. Biol. **57**, 7783–7797 (2012).

[8]C. M. Poole, I. Cornelius, J. V. Trapp, and C. M. Langton, "Radiotherapy Monte Carlo simulation using cloud computing technology," Phys. Med. Biol. **35**, 497–502 (2012).

[9]H. Miras, R. Jimenez, C. Miras, and C. Goma, "CloudMC: A cloud computing application for Monte Carlo simulation," Phys. Med. Biol. **58**, N125–N133 (2013).

[10]L. Jahnke, J. Fleckenstein, F. Wenz, and J. Hesser, "GMC: A GPU implementation of a Monte Carlo dose calculation based on GEANT4," Phys. Med. Biol. **57**, 1217–1229 (2012).

[11]A.-C. Knopf and A. Lomax, "*In vivo* proton range verification: A review," Phys. Med. Biol. **58**, R131–R160 (2013).

[12]P. Andreo, "On the clinical spatial resolution achievable with protons and heavier charged particle radiotherapy beams," Phys. Med. Biol. **54**, N205–N215 (2009).

[13]H. Paganetti, H. Jiang, S.-Y. Lee, and H. M. Kooy, "Accurate Monte Carlo simulations for nozzle design, commissioning, and quality assurance for a proton radiation therapy facility," Med. Phys. **31**, 2107–2118 (2004).

[14]B. Clasie, N. Depauw, M. Fransen, C. Goma, H. Reza Panahandeh, J. Seco, J. B. Flanz, and H. M. Kooy, "Golden beam data for proton pencil-beam scanning," Phys. Med. Biol. **57**, 1147–1158 (2012).

[15]J. Herault, N. Iborra, B. Serrano, and P. Chauvel, "Monte Carlo simulation of a proton therapy platform devoted to ocular melanoma," Med. Phys. **32**, 910–919 (2005).

[16]C. Baker, D. Shipley, H. Palmans, and A. Kacperek, "Monte Carlo modeling of a clinical proton beam-line for the treatment of ocular tumours," Nucl. Instrum. Methods Phys. Res., Sect. A **562**, 1005–1008 (2006).

[17]S. D. Randeniya, P. J. Taddei, W. D. Newhauser, and P. Yepes, "Intercomparison of Monte Carlo radiation transport codes MCNPX, GEANT4, and FLUKA for simulating proton radiotherapy of the eye," Nucl. Technol. **168**(3), 810–814 (2009).

[18]F. Romano, G. A. P. Cirrone, G. Cuttone, F. Di Rosa, S. E. Mazzaglia, I. Petrovic, A. R. Fira, and A. Varisano, "A Monte Carlo study for the calculation of the average linear energy transfer (LET) distributions for a clinical proton beam line and a radiobiological carbon ion beam line," Phys. Med. Biol. **59**, 2863–2882 (2014).

[19]M. F. Moyers, G. B. Coutrakon, A. Ghebremedhin, K. Shahnazi, P. Koss, and E. Sanders, "Calibration of a proton beam energy monitor," Med. Phys. **34**, 1952–1966 (2007).

[20]C. Castaneda, "Crocker nuclear laboratory (CNL) radiation effects measurement and test facility," in *IEEE Radiation Effects Data Workshop* (IEEE, Washington, DC, 2001), pp. 77–81.

[21]I. K. Daftari, T. R. Renner, L. J. Verhey, R. P. Singh, M. Nyman, P. L. Petti, and J. R. Castroa, "New UCSF proton ocular beam facility at the cracker nuclear laboratory cyclotron (UC Davis)," Nucl. Instrum. Methods Phys. Res., Sect. A **380**, 597–612 (1996).

[22]I. K. Daftari, C. M. Castaneda, T. Essert, T. L. Phillips, and K. K. Mishra, "Scintillator–CCD camera system light output response to dosimetry parameters for proton beam range measurement," Nucl. Instrum. Methods Phys. Res., Sect. A **686**, 7–14 (2012).

[23]P. Mobit, G. Sandison, and P. Bloch, "Depth ionization curves for an unmodulated proton beam measured with different ionization chambers," Med. Phys. **27**(12), 2780–2787 (2000).

[24]AAPM TG-21, "A protocol for the determination of absorbed dose from high-energy photon and electron beams," Med. Phys. **10**, 741–771 (1983).

[25]P. R. Almond, P. J. Biggs, B. M. Coursey, W. F. Hanson, M. S. Huq, R. Nath, and D. W. O. Rogers, "AAPM's TG-51 protocol for clinical reference dosimetry of high-energy photon and electron beams," Med. Phys. **26**, 1847–1870 (1999).

[26]P. Arce, P. Rato, M. Canadas, and J. I. Lagares, "GAMOS: A GEANT4-based easy and flexible framework for nuclear medicine applications," in *IEEE Nuclear Science Symposium Conference Record* (IEEE, Washington, DC, 2008), pp. 3162–3168.

[27]E. Grusell and J. Medin, "General characteristics of the use of silicon diode detectors for clinical dosimetry in proton beams," Phys. Med. Biol. **45**, 2573–2582 (2000).

[28]M. Pacilio, C. De Angelis, S. Onori, L. Azario, A. Fidanzio, R. Miceli, A. Peirmattei, and A. Kacperek, "Characteristics of silicon and diamond detectors in a 60 MeV proton beam," Phys. Med. Biol. **47**, N107–N112 (2002).

[29]C. Goma, P. Andreo, and J. Sempau, "Spencer-Attix water/medium stopping-power ratios for the dosimetry of proton pencil beams," Phys. Med. Biol. **58**, 2509–2522 (2013).

[30]C. Ross, M. McEwen, A. McDonald, C. Cojocaru, and B. Faddegon, "Measurement of multiple scattering of 13 and 20 MeV electrons by thin foils," Med. Phys. **35**(9), 4121–4131 (2008).

[31]J. Sorriaux, A. Kacperek, S. Rossomme, J. A. Lee, D. Bertrand, S. Vynckier, and E. Sterpin, "Evaluation of Gafchromic EBT3 films characteristics in therapy photon, electron, and proton beams," Phys. Med. **29**, 599–606 (2013).

[32]A. Carnicer, G. Angellier, A. Gerard, N. Garnier, C. Dubois, R. Amblard, and J. Herault, "Development and validation of radiochromic film dosimetry and Monte Carlo simulation tools for acquisition of absolute, high-spatial resolution longitudinal dose distributions in ocular proton therapy," Radiat. Meas. **59**, 225–232 (2013).

[33]S. Agostinelli *et al.*, "GEANT4: A simulation toolkit," Nucl. Instrum. Methods Phys. Res., Sect. A **506**, 250–303 (2003).

[34]A. Lechner, V. N. Ivanchencko, and J. Knobloch, "Validation of recent GEANT4 physics models for application in carbon ion therapy," Nucl. Instrum. Methods Phys. Res., Sect. B **268**, 2343–2354 (2010).

[35]T. Bortfeld, "An analytical approximation of the Bragg curve for therapeutic proton beams," Med. Phys. **24**(12), 2024–2033 (1997).

[36]International Commission in Radiation Units and Measurements, "Clinical proton dosimetry Part I: Beam production, beam delivery, and measurement of absorbed dose," ICRU Report No. 59 (ICRU Publications, Bethesda, Maryland, 1998).

[37]C. De Angelis, S. Onori, M. Pacili, G. A. Cirrone, G. Cuttone, L. Raffaele, and M. G. Sabini, "Preliminary results on a dedicated silicon diode detector for proton dosimetry," Radiat. Prot. Dosim. **101**, 461–464 (2002).